

# Diode Factor in Solar Cells with Metastable Defects and Back Contact Recombination

Taowen Wang,\* Florian Ehre, Thomas Paul Weiss, Boris Veith-Wolf, Valeriya Titova, Nathalie Valle, Michele Melchiorre, Omar Ramírez, Jan Schmidt, and Susanne Siebentritt

To achieve a high fill factor, a small diode factor close to 1 is essential. The optical diode factor determined by photoluminescence is the diode factor from the neutral zone of the solar cell and thus a lower bound for the diode factor. Due to metastable defects transitions, the optical diode factor is higher than 1 even at low excitation. Here, the influence of the backside recombination and the doping level on the optical diode factor are studied. First, photoluminescence and solar cell capacitance simulator (SCAPS) simulations are used to determine the back surface recombination velocity of Cu(In, Ga)Se<sub>2</sub> with various back contacts and different doping levels. Then, experimental results and simulations show that both back surface recombination and high doping density reduce the optical diode factor. The back surface recombination reduces the optical diode factor with undesirable extra nonradiative recombination. The smaller value achieved by higher doping can increase quasi-Fermi level splitting at the same time. The simulations show that the back surface recombination reduces the optical diode factor due to an illumination-dependent recombination rate. In addition, a higher majority carrier doping reduces the influence of majority carrier gain from metastable defect transitions, thus reducing the optical diode factor.

cells.<sup>[8,9]</sup> Besides the presence of metastable defects, the various nonradiative recombination channels in the bulk and at the interfaces of the absorber determine the efficiency. While it is well-known that increased non-radiative recombination reduces the open circuit voltage ( $V_{oc}$ ), the correlation between increased non-radiative recombination, e.g. at the back contact, and the diode factor is less obvious. Since in a complete device the factors influencing recombination and diode factor are numerous, it is thus desirable to study the absorber before finishing the solar cells.<sup>[10]</sup> As photoluminescence offers the possibility to study the quasi-Fermi level splitting, i.e., the open circuit voltage, as well as the diode factor of the bare absorbers,<sup>[10–12]</sup> it is thus possible to study the interplay between bulk recombination, back surface recombination, diode factor, and efficiency, before adding more complexity by introducing the contact layers.

## 1. Introduction

Many semiconductors used as absorbers in solar cells contain defects that show metastable behavior.<sup>[1–7]</sup> A prominent mechanism of such metastable transition is the transformation of donor states (acceptor states) into acceptor states (donor states) upon electron capture (release).<sup>[1]</sup> This transformation can result in an additional shift of the quasi-Fermi level of carriers, leading to an increase in the diode factor above 1, even for recombination in the neutral zone and at low injection, thereby decreasing the fill factor (FF) and efficiency of solar

The PL study of the absorber without contact layers results in the maximum open circuit voltage and the minimum diode factor, which the absorber is capable of. Adding the contact layers can introduce additional recombination channels, which reduces the open circuit voltage and increases the diode factor. Investigation of the absorber alone helps to disentangle the different effects.

Recombination not only influences the  $V_{oc}$  or  $\Delta E_F$  but also the fill factor of the solar cells via the diode factor, for which a small diode factor close to 1 is generally desirable.<sup>[8,9]</sup> For a sufficiently doped semiconductor in low injection conditions,

T. Wang, F. Ehre, T. P. Weiss, M. Melchiorre, O. Ramírez, S. Siebentritt  
Laboratory for Photovoltaics (LPV)  
Department of Physics and Materials Science  
University of Luxembourg  
41 rue du Brill, Belvaux L-4422, Luxembourg  
E-mail: taowen.wang@uni.lu

The ORCID identification number(s) for the author(s) of this article can be found under <https://doi.org/10.1002/aenm.202202076>.

© 2022 The Authors. Advanced Energy Materials published by Wiley-VCH GmbH. This is an open access article under the terms of the Creative Commons Attribution License, which permits use, distribution and reproduction in any medium, provided the original work is properly cited.

DOI: 10.1002/aenm.202202076

B. Veith-Wolf, V. Titova, J. Schmidt  
Institute for Solar Energy Research Hamelin (ISFH)  
Am Ohrberg 1, D-31860 Emmerthal, Germany  
N. Valle  
Luxembourg Institute of Science and Technology (LIST)  
Materials Research and Technology Department  
41 rue du Brill, Belvaux L-4422, Luxembourg  
J. Schmidt  
Institute of Solid-State Physics  
Leibniz University Hannover  
Appelstr 2, 30167 Hannover, Germany

both radiative recombination and trap-assisted Shockley-Read-Hall (SRH) recombination in the quasi-neutral region (QNR) can only shift the minority carrier quasi-Fermi level, leading to a diode factor of 1.<sup>[13]</sup> A diode factor of 2 is generally due to recombination taking place in the space charge region (SCR) which is depleted and thus both quasi-Fermi levels shift with increasing injection levels.<sup>[13]</sup> Generally, the diode factor is determined from the dark current density–voltage ( $J_d$ – $V$ ) characteristic, which is labeled as the electrical diode factor (EDF).<sup>[9,14,15]</sup> Depending on the recombination mechanism, the EDF is between 1 and 2. The dominating recombination channel can be judged from the value of the EDF or from a fit to a two-diode model. In nonideal cases, the  $J_d$ – $V$  characteristics can be dominated by series and shunt resistance, making it problematic to extract the reliable diode factor.<sup>[14]</sup> To remove puzzling influences from series and shunt resistance, illumination intensity-dependent photoluminescence allows us to extract the reliable optical diode factor (ODF) of the contactless absorbers at open-circuit conditions.<sup>[12,16–18]</sup> Another available technology is Suns- $V_{oc}$  measurement which measures the  $V_{oc}$  of finished devices depending on illumination intensity. It avoids the influence of the series resistance and gives generally more reliable results for the diode factor of the finished device. It was shown in the literature that, in the absence of dominating SCR or contact recombination, the Sun- $V_{oc}$  diode factor has a very good agreement with Suns (illumination intensity)-PL measurement, i.e., with the optical diode factor.<sup>[18]</sup> The relation between EDF and ODF has been discussed in earlier works:<sup>[18–20]</sup> they are equivalent in the situation when the finished devices do not have additional recombination paths compared to the contactless absorbers, i.e., when the device is dominated by recombination in the quasi-neutral zone. Essentially, in a  $J$ – $V$  measurement, a voltage is applied and the resulting current is measured. In an excitation-dependent PL intensity measurement, the generation flux (i.e., the current) is defined by the experimental condition and the quasi-Fermi level splitting (i.e., the voltage) is measured because the PL intensity is proportional to the exponential of the open circuit voltage/quasi-Fermi level splitting.<sup>[21,22]</sup> Since there is a very weak or even no space charge region in contactless absorbers, the ODF is the diode factor of the QNR. Theoretically, the ODF from the QNR of a doped semiconductor is supposed to be 1 in low injection conditions because the excited free carrier can only shift the Fermi level of minority carriers. However, it is usually observed experimentally that the ODF is larger than 1 in low injection conditions. This observation is explained by metastable defects converting from donors to acceptors (or acceptors to donors) that additionally shift the Fermi level of majority carriers.<sup>[8]</sup> This metastable transition is a balanced system of forward and backward transformation that is injection level or  $\Delta E_F$  depended. The time constants of this transition are sufficiently short in the range of a couple of seconds as we reported before,<sup>[8]</sup> which means the metastable defects influence the diode factor when tracking maximum working point (MPP) with typical scan speeds. It also means that in a (slow enough) quasi-steady state measurement of  $J$ – $V$  or PL the metastable defects are in a quasi-equilibrium state, which depends on the applied voltage or generation flux. The theory of the ODF due to metastable defects transition can be extended by considering the influence of back surface

recombination and doping density, making the ODF an even more versatile contactless and non-destructive optical characterization method to predict the efficiency of solar cells.

In this contribution, we focus on copper indium gallium selenide [Cu(In, Ga)Se<sub>2</sub>] solar cells, because their metastable defects have a profound influence on the diode factor. Additionally, it has been demonstrated that mitigating back surface recombination and improving doping level in this material is critical to achieving high power conversion efficiencies. CuInSe<sub>2</sub> solar cells with Mo back contact have a high surface recombination velocity of more than 10<sup>5</sup> cm s<sup>−1</sup>.<sup>[23–25]</sup> In the first part of this work, different strategies such as Ga back grading (GBG)<sup>[26–29]</sup> or dielectric layers<sup>[30–33]</sup> are used to passivate the back contact. In addition, the doping levels of these absorbers are controlled by changing the composition (Cu/In atomic ratio). Photoluminescence and solar cell capacitance simulator (SCAPS) simulations are used to determine back surface recombination velocity and doping density. This approach allows us to quantitatively study the influence of back surface recombination velocity and doping density on the diode factor by using photoluminescence and simulations, which further allows us to quantitatively study the influence on quasi-Fermi level splitting ( $\Delta E_F$ ), i.e., the  $V_{oc}$ , in addition to the diode factor. In the following we demonstrate that samples with unpassivated back contacts show a lower  $\Delta E_F$  and a smaller ODF, indicating that back surface recombination reduces not only the  $\Delta E_F$ , as expected, but also the diode factor. SCAPS simulations clarify the mechanism by which back surface recombination reduces the diode factor: the diffusion of minorities towards the back contact leads to a sublinear increase of the electron concentration with illumination. On the other hand, due to the higher majority carrier reservoir, a smaller diode factor can also be the result of sufficient doping that contributes simultaneously to the higher  $\Delta E_F$  and hence the higher  $V_{oc}$ . SCAPS simulations show similar results to experiments, which confirms that the ODF > 1 is caused by the extra increase in the majority carrier density due to illumination-dependent metastable defects transformation. We discuss how the ODF measurements comparing different samples can indicate whether the differences are due to back surface recombination or doping density of the absorbers.

## 2. Results and Discussion

### 2.1. The Effects of Back Surface Recombination on $\Delta E_F$

Both SCAPS<sup>[34]</sup> simulations and experiments are conducted to investigate the influence of back surface recombination and doping density on  $\Delta E_F$ . Based on that, we can quantify the back surface recombination velocity and doping density, which then allows us to understand the correlation between back surface recombination velocity, doping density, and the ODF. SCAPS is a 1D modeling solar cell simulator that is optimized for thin film solar cells. All parameters used in the simulations can be found in Table S1 (Supporting Information). To set the scene, we investigate in **Figure 1a** quasi-Fermi level splitting of a CuInSe<sub>2</sub> absorber as a function of back surface recombination velocity ( $S_b$ ) and bulk lifetime ( $\tau_b$ ) based on SCAPS simulations. Here, the front surface recombination velocity is fixed at

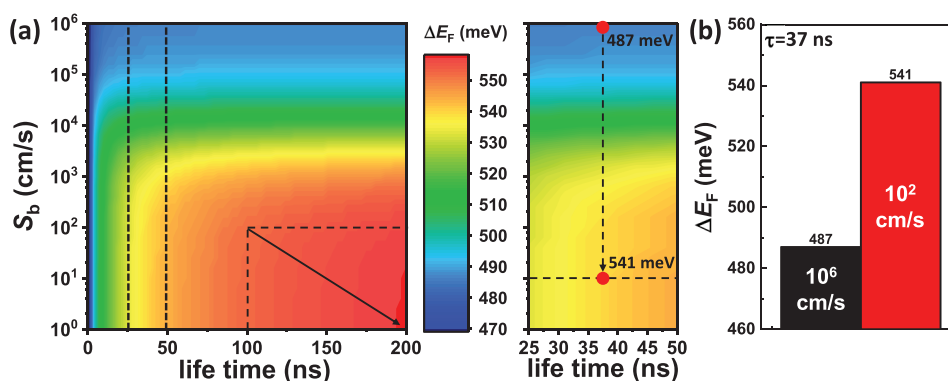


**Figure 1.** a) With doping density  $N_A$  of  $1 \times 10^{16}$  cm $^{-3}$ , film thickness of 3  $\mu$ m, electron mobility of 100 cm $^2$  V $^{-1}$  s $^{-1}$  and front surface recombination velocity of  $1.4 \times 10^3$  cm s $^{-1}$ , the SCAPS simulated  $\Delta E_F$  increases with decreasing back surface recombination velocity and increasing minority carrier lifetime. Due to the limitation of front surface recombination, further decreasing  $S_b$  and increasing bulk lifetime along the black arrow in the lower right corner can only slightly increase  $\Delta E_F$ . The second figure is an enlargement of the first figure range from 25 to 50 ns. b) With an approximate bulk lifetime of 37 ns, around 50 meV  $\Delta E_F$  can be improved by reducing the back surface recombination velocity from  $10^6$  to  $10^2$  cm s $^{-1}$ .

$1.4 \times 10^3$  cm s $^{-1}$  as it has been found experimentally for the CdS covered the front surface of Cu(In, Ga)Se $_2$  absorbers.<sup>[23]</sup> We assume that the recombination velocity on a CuInSe $_2$  surface (without Ga) is similar. In a typical  $\tau_b$  range of Cu(In, Ga)Se $_2$  solar cells from 25 to 50 ns,<sup>[35,36]</sup> the highest  $\Delta E_F$  of  $\approx 545$  meV can be achieved with a lifetime of 50 ns and a back surface recombination velocity lower than  $10^2$  cm s $^{-1}$ . With more advanced deposition technologies or alkali element post-deposition treatment (PDT),  $\tau_b \geq 200$  ns can be achieved,<sup>[37–41]</sup> which leads to the highest  $\Delta E_F$  of 560 meV. Again we assume that we can transfer typical lifetime values measured from Cu(In, Ga)Se $_2$  to our CuInSe $_2$  absorbers. For the samples studied in our experiments, the longest  $\tau_b$  was determined to be 37 ns (see below). With this lifetime, the simulation (Figure 1b) predicts a  $\Delta E_F$  gain of  $\approx 50$  meV by reducing  $S_b$  from  $10^6$  to  $10^2$  cm s $^{-1}$  even for thick absorbers. When the  $\tau_b$  is long enough to make minority carrier diffusion length comparable to absorber thickness (around 50 ns in our case with electron mobility  $\mu_n = 100$  cm $^2$  V $^{-1}$  s $^{-1}$ <sup>[42]</sup> and film thickness of 3  $\mu$ m), the back surface recombination becomes the main issue that controls  $\Delta E_F$ . In terms of the front surface, we assume a rather benign front surface recombination velocity, as mentioned above. However, compared to back surface recombination, front surface recombination has an even stronger influence on  $\Delta E_F$  because most of the photons are absorbed in the region close to the front surface. As a result,  $\Delta E_F$  stays nearly the same when the  $\tau_b$  is longer than 100 ns and  $S_b < 10^2$  cm s $^{-1}$  as shown in Figure 1a with a black arrow. In this case, the  $\Delta E_F$  deficits are dominated by front surface recombination. The details about the influences of front surface recombination on  $\Delta E_F$  are discussed (Figure S1, Supporting Information). It shows that another 40 meV improvement of  $\Delta E_F$  can be achieved by reducing the front surface recombination velocity from  $1.4 \times 10^3$  to  $10^0$  cm s $^{-1}$ .

To verify the prediction of the SCAPS simulations and obtain different back surface recombination velocities experimentally, both dielectric metal oxide layers and GBG passivation are applied. The sample structures studied in experiments are shown in Figure 2a. We prepared 4 samples coming from the same deposition process to study the passivation effects of

dielectric layers. The first one is a reference CuInSe $_2$  grown on Mo-coated soda-lime glass without any back contact passivation. The second one is grown directly on clean soda-lime glass. Another two are passivated by 5 nm Al $_2$ O $_3$  or 4 nm TiO $_2$ , respectively. All the samples are covered by CdS to reduce front surface recombination and stabilize the front surface.<sup>[43,44]</sup> Another four samples were prepared to study the passivation effects of the GBG. All the samples are grown on Mo-coated soda-lime glass and passivated with a CdS layer at the front surface. The reference sample is a pure CuInSe $_2$  without any Ga. The other three samples have different Ga depth profiles that are realized by controlling the substrate temperature and Ga supply duration. 6m-540, 6m-590 or 8m-590 means that the sample experiences 6/6/8 min predeposition of CuGaSe $_2$  then followed by CuInSe $_2$  deposition with the highest substrate temperature of 540/590/590  $^{\circ}$ C. The highest growth temperature of the reference sample is 590  $^{\circ}$ C. The GGI and corresponding  $E_g$  depth distribution, shown in Figure 2c, is determined by noncalibrated secondary ion mass spectrometry (SMIS) and PL. Details about determining GGI distribution based on these two technologies are shown (Section S3, Supporting Information; see Figure S2, Supporting Information). The left y-axis in Figure 2c shows the bandgap  $E_g$  determined by the linear approximate dependency:  $E_g^{\text{GIS}} = E_g^{\text{GIS}} + 0.65$  (GGI), given in the reference.<sup>[45]</sup> For the applicability of the linear approximation, in Figure S3 (Supporting Information). The 8m-590 sample has the highest GGI and corresponding  $E_g$  at the backside due to the largest amount of Ga supply. The  $E_g$  of the 6m-540 sample is higher than the 6m-590 sample because a lower substrate temperature reduces the diffusion of Ga and thus flattens the profile. The film thickness difference shown in Figure 3c is due to the inhomogeneity of the film. To complete solar cells for GBG samples, sputtered i-ZnO/AZO and e-beam evaporated Al/Ni grids are deposited in sequence. More details about sample preparation can be found in the experimental section.

Figure 3a shows the absolute one-Sun PL spectra of all samples after annealing in the air. Rapid low-temperature annealing of Cu(In, Ga)Se $_2$  devices in the air was demonstrated to improve  $V_{oc}$  up to  $\approx 60$  mV.<sup>[46,47]</sup> For our films covered only with CdS, the improvement of  $\Delta E_F$  by  $\approx 30$  meV was also

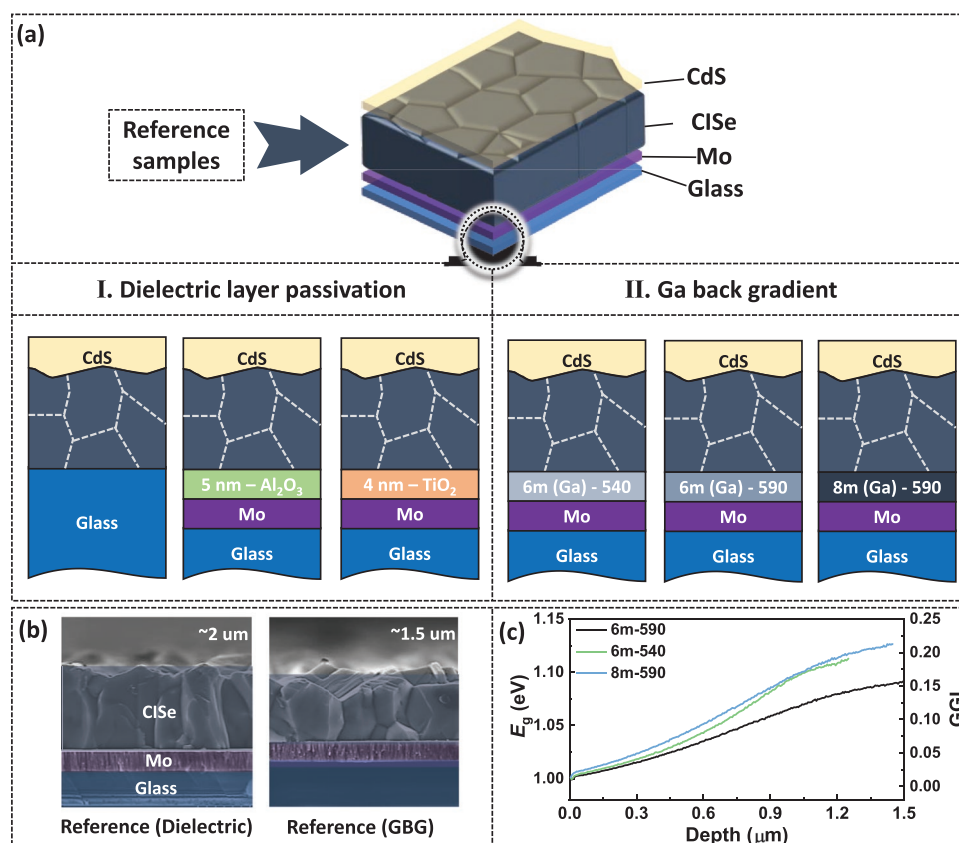


**Figure 2.** a) Reference CuInSe<sub>2</sub> sample grown directly on Mo. Dielectric layer passivated CuInSe<sub>2</sub> grown on soda-lime glass, 5 nm Al<sub>2</sub>O<sub>3</sub> or 4 nm TiO<sub>2</sub> respectively. Different Ga back gradient passivated CuInSe<sub>2</sub> samples grown with a 6/6/8 min CuGaSe<sub>2</sub> pre-deposition followed by a CuInSe<sub>2</sub> growth with the highest substrate temperature reaching 540/590/590 °C, respectively. The samples were covered with CdS before measuring PL. b) The SEM cross-section of reference bare absorbers. The thickness of absorbers is ≈2.0 μm and ≈1.5 μm for dielectric layer passivated (left) and GBG passivated (right) samples, respectively. c) GGI and corresponding E<sub>g</sub> depth profiles for GBG samples, which are extracted from noncalibrated SIMS and PL.

confirmed after 200 °C and 2 min of annealing in the air. The results of samples without annealing are shown in Figure S4 (Supporting Information). For the absolute PL, a higher radiation flux means less nonradiative recombination loss, thus a

higher  $\Delta E_F$ .  $\Delta E_F$  shown in Figure 3b is determined by a fit to Planck's generalized law.<sup>[11,48]</sup> With the passivation of the dielectric layer and GBG,  $\Delta E_F$  is improved compared to the reference sample. Inserting a 5 nm ALD Al<sub>2</sub>O<sub>3</sub> layer achieves the

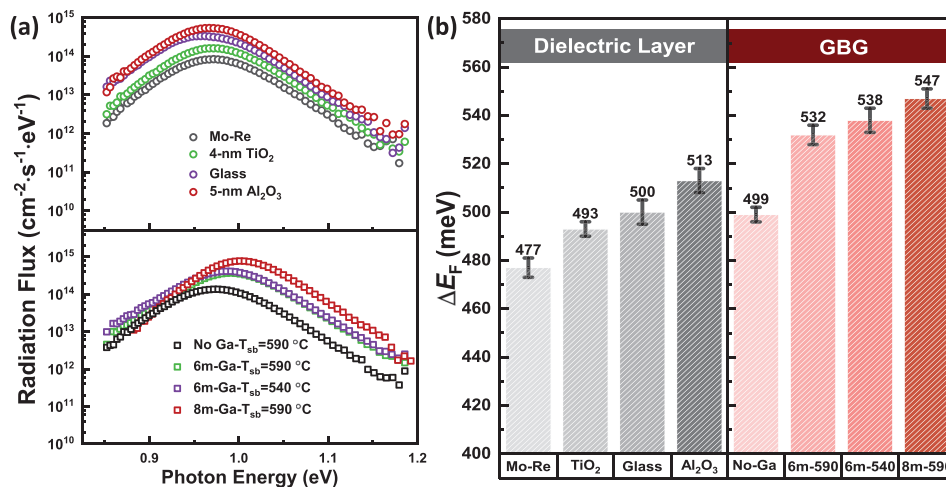


**Figure 3.** a) The absolute one-Sun PL spectra of dielectric layers and GBG passivated samples with annealing in the air. b) Compared to the unpassivated reference samples, the  $\Delta E_F$  is improved after introducing a dielectric layer or Ga back gradient.



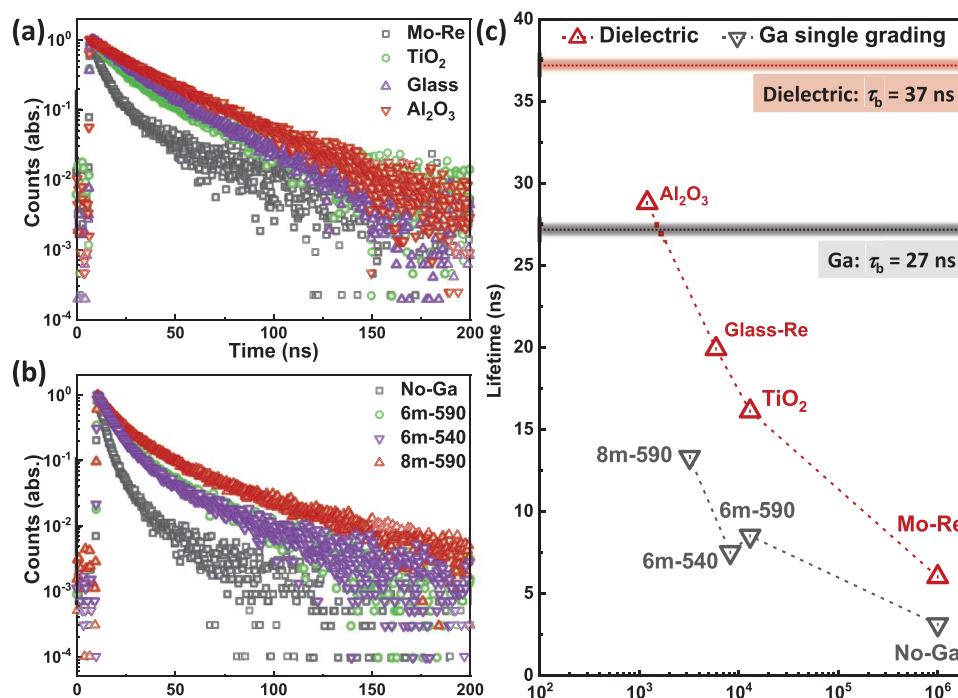


**Figure 4.** TRPL decay of samples after annealing in the air: a) The PL counts decay of the dielectric layer or glass passivated samples compared to the unpassivated sample. b) The PL counts decay of the GBG samples compared to the reference sample without Ga gradient. c) The effective lifetime decreases with increasing back surface recombination velocity. The lifetime shown here is a weighted effective lifetime that is determined by a 2-exponential decay fitting. The back surface recombination velocities are extracted by SCAPS simulations (see Figure 5).

highest  $\Delta E_F$  improvement of  $\approx 40$  meV among dielectric layer passivated samples. It implies that Al<sub>2</sub>O<sub>3</sub> is most effective to suppress back surface recombination among the studied dielectric layers, as observed previously.<sup>[33,49]</sup> A similar  $\Delta E_F$  gain of  $\approx 40$  meV is obtained from the GBG samples, which means that the passivation effect of GBG is comparable to Al<sub>2</sub>O<sub>3</sub> which has been widely applied in various semiconductor devices to reduce surface recombination.<sup>[50–52]</sup>  $\Delta E_F$  of dielectric layer passivated samples are lower than GBG samples because they have lower doping density as will be discussed later. Our results also show that back surface recombination is important, even in thick absorbers.

To quantitatively determine the back surface recombination velocity, we will compare the measured  $\Delta E_F$  with SCAPS simulations (see Figure 5). For relevant simulations, it is essential to know the bulk lifetime and doping density of the samples. Both of them can be estimated from PL, as we discuss in the following. Firstly, the bulk lifetime is described by:

$$\frac{1}{\tau_n^{\text{eff}}} = \frac{1}{\tau_b} + \frac{1}{\tau_s} \quad (1)$$

where  $\tau_n^{\text{eff}}$  is the effective (measured) minority carrier lifetime,  $\tau_b$  is the bulk lifetime and  $\tau_s$  is the surface lifetime

**Table 1.** Efficiency,  $V_{oc}$ ,  $\Delta E_F$ , lifetime, doping density and (effective) back surface recombination velocity.

Sample	$V_{oc}$ [mV]	$\Delta E_F$ [meV]	Lifetime [ns]	$N_A$ [cm <sup>-3</sup> ]	$S_b$ -analytical [cm s <sup>-1</sup> ]	$S_b$ -Equation (4) [cm s <sup>-1</sup> ]	$S_b$ -SCAPS [cm s <sup>-1</sup> ]
8m-590 Ga	524	547	13.3	$1.9 \times 10^{16}$	$4.5 \times 10^3$	$6.2 \times 10^3$	$3.2 \times 10^{3a)}$
6m-590 Ga	503	532	8.5	$1.7 \times 10^{16}$	$1.4 \times 10^4$	$4.3 \times 10^4$	$1.3 \times 10^{4a)}$
6m-540 Ga	525	538	7.5	$2.4 \times 10^{16}$	$1.8 \times 10^4$	$9.2 \times 10^3$	$8.2 \times 10^{3a)}$
No-Ga Re	453	499	3.4	$1.9 \times 10^{16}$	$1.0 \times 10^6$	$1.0 \times 10^6$	$1.0 \times 10^6$
Al <sub>2</sub> O <sub>3</sub>	/	513	28.8	$7.8 \times 10^{15}$	$3.0 \times 10^3$	/	$1.2 \times 10^3$
Glass		501	19.9	$8.6 \times 10^{15}$	$3.7 \times 10^3$		$5.9 \times 10^3$
TiO <sub>2</sub>		493	16.1	$7.2 \times 10^{15}$	$6.9 \times 10^4$		$1.3 \times 10^4$
Mo		477	6.0	$7.6 \times 10^{15}$	$1.0 \times 10^6$		$1.0 \times 10^6$

<sup>a)</sup>The  $S_b$  of the GBG sample is an effective surface recombination velocity.

due to front and back surface recombination. The  $\tau_n^{\text{eff}}$  of air-annealed samples is determined by TRPL measurements, as shown in Figure 4a,b. Because some samples show 2-exponential decay, the 2-exponential fitting is used to determine the weighted effective lifetimes according to Equation (8) (experimental section) and the results are summarized in Table 1. More details of 2-exponential fitting can be found in Table S3 (Supporting Information). The  $\text{Al}_2\text{O}_3$  passivated sample shows the slowest decay with an effective minority carrier lifetime of 28.8 ns which is nearly five times longer than that of the unpassivated sample. Assuming that in the steady state the carriers are uniformly distributed, 40 meV gain in  $\Delta E_F$  can be estimated according to  $k_B T \cdot \ln\left(\frac{\tau_1}{\tau_2}\right)$ , where  $k_B T$  is the thermal energy at measured temperature,  $\tau_1$  and  $\tau_2$  are effective minority carrier lifetimes with and without passivation, respectively.<sup>[11]</sup> It agrees with the gain in PL-determined  $\Delta E_F$  which leads to the highest  $\Delta E_F$  of 513 meV. Similar but a bit lower passivation effects are also observed for  $\text{TiO}_2$  and glass with a somewhat shorter effective lifetime of 16.1 ns and 19.9 ns. The longer lifetimes of the GBG passivated samples are also confirmed. The 8m-590 sample has the longest lifetime of 13.3 ns, which means the lowest back surface recombination, leading to the highest  $\Delta E_F$  of 547 meV. The best passivation originates from the highest conduction band minimum at the back contact (see Figure 2c), which lowers back surface recombination by reducing electron density (minority carrier density). As expected, the 6m-590 sample has the lowest conduction band minimum at the backside which results in a shorter lifetime of 8.5 ns. However, the minority carrier lifetime of the 6m-540 sample is slightly shorter than the 6m-590 sample, even with a higher conduction band minimum at the backside. We believe this is because the higher growth temperature increases absorber quality, which leads to a longer bulk minority carrier lifetime.<sup>[53]</sup>

For the unpassivated sample, the back surface recombination velocity between Mo and  $\text{CuInSe}_2$  ( $10^6 \text{ cm s}^{-1}$ )<sup>[24,25]</sup> is much higher than that of the  $\text{CdS}$ -covered front surface ( $1.4 \times 10^3 \text{ cm s}^{-1}$ ).<sup>[23]</sup> In the case where one surface of a thin film is much more recombination active than the other one, the following relation was derived to estimate surface lifetime:<sup>[54]</sup>

$$\tau_s \cong \frac{d}{S_b} + \frac{4}{D} \left( \frac{d}{\pi} \right)^2 \quad (2)$$

where  $d$  is the film thickness,  $S_b$  is the back surface recombination velocity and  $D$  is the diffusion constant of the minority carriers.  $D$  is determined by the Einstein relation,  $D = \frac{\mu_e k_B T}{q}$ ,  $q$  is elementary charge and  $\mu_e$  is electron mobility.  $\mu_e = 100 \text{ cm}^2 \text{ V}^{-1} \text{ s}^{-1}$  is used for Equation (2) and SCAPS simulations.<sup>[42]</sup> Similar values of  $\mu_e$  were found in Hall measurements on epitaxial n-type films.<sup>[55]</sup> The thicknesses of samples are determined by SEM cross sections, as shown in Figure 2b. Then by introducing Equation (2) into Equation (1), the approximated bulk lifetimes of the reference samples for the dielectric layer series and the GBG passivated series are calculated

from the effective lifetimes  $\tau_n^{\text{eff}}$ . The bulk lifetime of the reference sample of the GBG series and the dielectric layer passivated series is determined to be 27 ns and 37 ns, respectively. We assume in the following that the back surface passivation does not change the bulk lifetime. This assumption may be somewhat problematic for the 6m-540 sample, as it was grown at a lower temperature, but for the dielectric layer series, which were grown in the same process, this assumption is well justified. We can thus use the bulk lifetime to extract the surface recombination lifetime of the passivated samples using Equation (1). However, Equation (2) is no longer applicable to extract the back surface recombination velocity of the passivated samples, because the front and back surface recombination velocities become comparable (see the discussion in Section S9 and Figure S8, Supporting Information). Thus, we use SCAPS simulations to numerically determine the back surface recombination velocity.

As doping density is necessary for SCAPS simulations (and further discussion of its influence on the ODF), it is estimated from the quasi-Fermi level splitting and the effective lifetime using the following equation (see Section S7, Supporting Information for the derivation):

$$N_A = p_0 = \frac{d \cdot N_c N_v}{G \cdot \tau_n^{\text{eff}}} \exp\left(\frac{\Delta E_F - E_g}{k_B T}\right) \quad (3)$$

where  $N_c$  and  $N_v$  are the effective density of states of the conduction and valence band, respectively.  $\tau_n^{\text{eff}}$  is the effective carrier lifetime obtained from TRPL measurements.  $G$  is the generation flux during the steady state  $\Delta E_F$  measurement and  $d$  is the thickness of the film. It is a contactless optical method to extract the doping density, whereas the classical capacitance–voltage (C–V) or Hall measurements need a junction or at least contacts. To calculate the doping density shown in Table 1, we assume a homogeneous distribution of electrons for all samples including the GBG ones without considering the electron confinement due to the bandgap gradient. The simulations (Section S8 and Figure S6, Supporting Information) show that the confinement effect is weak: only  $\approx 10$  meV of  $\Delta E_F$  improvement can be achieved by introducing a similar conduction band gradient to the experimentally determined gradient. The doping density of the GBG samples and their reference is  $\approx 1.8 \times 10^{16} \text{ cm}^{-3}$  which is higher than the doping density of the dielectric passivated samples of  $\approx 8.0 \times 10^{15} \text{ cm}^{-3}$ . The higher doping density is most likely caused by the composition difference among these absorbers because the Cu ratio (Cu/In) of the dielectric layer passivated series is around 0.87, much lower than the 0.96 (Cu/In+Ga) of GBG samples. Earlier works have shown that a higher Cu content increases p-type doping.<sup>[56,57]</sup> This is because the Cu-poor samples have a higher density of shallow donor  $\text{In}_{\text{Cu}}$  antisite defects that decrease the p-type doping.<sup>[58,59]</sup> But on the other hand, the more Cu-poor  $\text{Cu(In, Ga)Se}_2$  seems to have a longer minority carrier lifetime (the dielectric layer passivated sample series in Table 1) as reported by previous studies.<sup>[60]</sup> This explains why dielectric layer passivated Cu-poor samples have a longer minority carrier lifetime but a lower  $\Delta E_F$  when compared to GBG samples. It may seem surprising that the doping density of the samples with a dielectric layer ( $\text{Al}_2\text{O}_3$  or  $\text{TiO}_2$ ) is very similar to the samples grown directly on glass or glass-Mo because

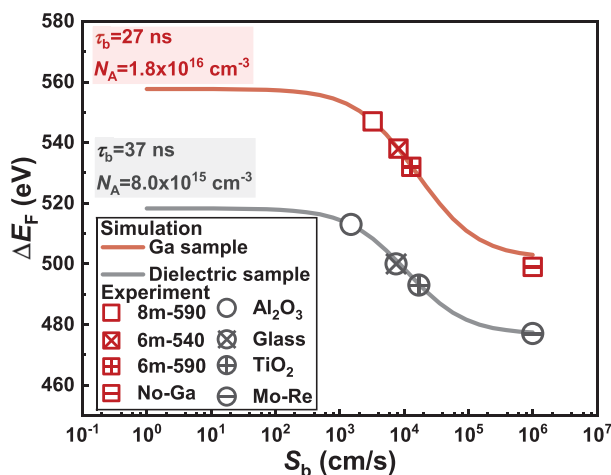


**Figure 5.** The solid lines are simulated  $\Delta E_F$  with respect to  $S_b$ . Black circles/red squares are measured  $\Delta E_F$  of dielectric layers/GBG passivated samples with their unpassivated reference. The  $S_b$  of the actual samples can be estimated by comparing the experimental  $\Delta E_F$  to the simulated results.

it can block the diffusion of alkalis that are responsible for the p-type doping in Cu(In, Ga)Se<sub>2</sub>. We believe that this is because the doping in the samples without the dielectric layer is already rather low. And the diffusion of Na also depends on growth conditions, e.g. the substrate temperature. Our maximum substrate temperature is 590 °C which is much higher than 540 °C in the reference that shows a blocking effect of dielectric layers for alkali diffusion.<sup>[61]</sup> To quantify the back surface recombination velocity from the SCAPS simulations, the experimentally determined doping density and bulk lifetime are involved to simulate  $\Delta E_F$  as a function of different back surface recombination velocities as shown in **Figure 5**. The  $\Delta E_F$  difference between the two curves ( $\approx 40$  meV) is larger than the expectation from the difference in doping density and bulk lifetime which is approximately 18 meV ( $k_B T \ln 2$ ). This is because the bandgap of the GBG samples (8m-590: 1.00 eV) used in simulations is higher than that of the dielectric samples (Mo Re: 0.975 eV). These differences are motivated and justified by the different PL peak energies among the samples (see Figure 3). Furthermore, the bandgap differences are also considered when we calculate the doping density according to Equation (3). Evidently, the simulations show that  $\Delta E_F$  decreases with higher recombination velocities. By comparing the  $\Delta E_F$  acquired in experiments and SCAPS simulations, the back surface recombination velocities of the different samples can be estimated and the results are summarized in Table 1. To be clear about how we arrive at the values for the backside recombination velocity, we summarize the workflow here:

1. We assume a surface recombination velocity of  $1.4 \times 10^3 \text{ cm s}^{-1}$  for the interface with CdS and  $10^6 \text{ cm s}^{-1}$  for the Mo interface, based on literature values. Using Equations (1) and (2) to determine the bulk lifetime of the (unpassivated) reference samples. We assume that back surface passivation does not influence the bulk lifetime.
2. We use Equation (3) to determine the doping density of all samples from the measured effective lifetime and quasi-Fermi level splitting.

3. With the bulk lifetime and doping densities from (1) and (2), SCAPS gives us a correct prediction of the quasi-Fermi level splitting of the reference samples, again assuming a backside recombination velocity of  $10^6 \text{ cm s}^{-1}$ . We can then vary the back side recombination velocity in SCAPS and obtain the quasi-Fermi level splitting (curves in Figure 5). Comparing the measured quasi-Fermi level splitting of the passivated samples with the simulated curves gives us the actual back surface recombination velocity of each sample.

The determined backside recombination velocity for the GBG samples is an effective one: i.e., the variable backside recombination velocity in simulations effectively reproduces the impact of the GGI gradient. The back surface recombination ( $U_s$ ) is given by  $U_s \approx S_b \Delta n$ ,  $\Delta n$  is the minority carrier (electron) density. The Ga gradient reduces back surface recombination by reducing  $\Delta n$  rather than reducing the surface defects density or their capture cross-section that determines  $S_b$ . The change of  $\Delta n$  depends on the difference in conduction band minimum ( $\Delta\phi$ ) at the backside between no Ga and Ga samples. Therefore, the backside recombination rate of graded samples ( $U_s^{\text{gra}}$ ) can also be expressed as:

$$U_s^{\text{gra}} \approx S_b \Delta n_{\text{gra}} = S_b \Delta n_{\text{flat}} \exp\left(\frac{-\Delta\phi}{k_B T}\right) = S_b^{\text{eff}} \Delta n_{\text{flat}} \quad (4)$$

where  $\Delta n_{\text{gra}}$  and  $\Delta n_{\text{flat}}$  is the minority carrier density of GBG and no Ga samples,  $S_b^{\text{eff}}$  is an effective back surface recombination velocity that is equal to  $S_b \exp\left(\frac{-\Delta\phi}{k_B T}\right)$ . The  $\Delta\phi$  (Figure 2c)

determined effective recombination velocities are compared in Table 1. The results agree well with the values obtained from the simulations. Furthermore, an analytical approach based on front and back side recombination is presented here with a similar agreement. The details of this approach are shown in Supporting Information 9. In terms of effective recombination velocity, the passivation effects of dielectric layers and GBG can be easily compared. For the dielectric layer passivation, Al<sub>2</sub>O<sub>3</sub> gives the lowest  $S_b = 1.2 \times 10^3 \text{ cm s}^{-1}$  resulting in the highest  $\Delta E_F$  and longest minority carrier lifetime. A similar but slightly lower passivation effect of the glass back contact ( $S_b = 5.9 \times 10^3$ ) is observed. The  $S_b$  of the TiO<sub>2</sub> sample is higher at  $1.3 \times 10^4 \text{ cm s}^{-1}$ , corresponding to another loss of 20 meV in  $\Delta E_F$  compared to the Al<sub>2</sub>O<sub>3</sub> sample. All dielectric layers show a considerable decrease of  $S_b$  compared to the unpassivated reference sample, demonstrating good passivation effects of dielectric layers. Similar passivation effects are observed for the GBG samples. The 8m-590 sample has the lowest effective  $S_b$  of  $3.2 \times 10^3 \text{ cm s}^{-1}$  which is only a bit higher than the Al<sub>2</sub>O<sub>3</sub> sample, which suggests the passivation effect of the Ga gradient is comparable to the Al<sub>2</sub>O<sub>3</sub>.

Because the dielectric layers usually block the current of devices,<sup>[62,63]</sup> complete solar cells are only prepared for GBG samples. By introducing the GBG, the 6m-540 sample achieves the highest efficiency of 15.7% without alkalis metal element PDT, clearly improved compared to the reference sample with the best efficiency of 13.1%. The lower efficiency of the 8m-590

and 6m-590 sample compared to the reference sample may be caused by the unoptimized deposition process of Cu(In, Ga)Se<sub>2</sub> that results in a dramatic loss of fill factor as shown in Figure S9b,c (Supporting Information). More results about devices can be found in Section S10 (Supporting Information).

Back surface recombination and doping density have strong influences on solar cells' efficiency. Both dielectric layers and GBG are effective to reduce back surface recombination thus resulting in a longer minority carrier lifetime and higher  $\Delta E_F$ . Minority carrier lifetime and  $\Delta E_F$  are applied to estimate the doping density of the absorbers. The higher doping density of GBG series explains their higher  $\Delta E_F$  compared to dielectric layer passivated series. The values of the back surface recombination velocities of these samples are quantified numerically and analytically based on absolute PL and TRPL. These data allow us now to study the influence of back surface recombination velocity and doping density on the ODF, to better understand the influence of the various recombination mechanisms on the ODF.

## 2.2. Optical Diode Factor (ODF)

### 2.2.1. Background

The diode factor has a significant influence on the performance of solar cells. Keeping everything else the same, a smaller diode factor (close to 1) is preferable because it results in a higher fill factor and thus improves the efficiency of the solar cells. The ODF determined by PL in this work is the diode factor of the absorber alone in absence of the PN-junction and therefore the diode factor of the QNR. In the case of an intrinsic absorber ( $n \approx p$ ), e.g., perovskite,<sup>[64]</sup> both quasi-Fermi levels of electrons ( $E_{Fn}$ ) and holes ( $E_{Fp}$ ) are shifted with excitation, which results in the ODF close to 2. For the p-type Cu(In, Ga)Se<sub>2</sub> with a general doping density of more than  $10^{15} \text{ cm}^{-3}$ ,<sup>[65]</sup> the  $\Delta E_F$  in low injection conditions is entirely due to the shift of  $E_{Fn}$ , leading to an ODF of 1.<sup>[17]</sup> However due to injection-dependent metastable defect transition, the ODF of the QNR of doped semiconductors can be larger than 1 in low injection conditions, as recently shown by Weiss.<sup>[8]</sup> Here, we recapture the critical points and equations that are needed to have a better understanding of our experiment and simulation results. The radiation flux  $R_t$  is empirically found to follow a power law over many orders of generation flux (given by the illumination intensity)  $G$ ,  $R_t \propto G^A$ . The exponent  $A$  is the ODF and is directly determined by the derivation of the logarithmic Radiation-Generation characteristic, which is:<sup>[8]</sup>

$$A = \frac{d \ln R_t}{d \ln G} = \frac{d \ln N_A}{d \ln G} + \frac{d \ln n}{d \ln G} \quad (5)$$

For Cu(In, Ga)Se<sub>2</sub>, it has been shown before that the TRPL decay time does not significantly change upon injection level by roughly 2 orders of magnitude.<sup>[23]</sup> Under the assumption that the minority carrier density  $\Delta n$  increases linearly with  $G$ , and  $\tau_n^{\text{eff}}$  is constant, the  $\Delta n$  can be determined by:

$$\Delta n = \frac{G \cdot \tau_n^{\text{eff}}}{d} \quad (6)$$

Combine Equations (5) and (6), we get:

$$A = \frac{d \ln R_t}{d \ln G} = 1 + \frac{d \ln N_A}{d \ln G} \quad (7)$$

More details of the derivation are shown in Section S11 (Supporting Information).<sup>[8]</sup> For doped semiconductors, the ODF depends on changes in the doping density  $N_A$  upon illumination, which can be explained by metastable defects.<sup>[1,8]</sup> If there were no metastable defect transitions,  $\frac{d \ln N_A}{d \ln G} = 0$ , which gives  $A = 1$  in low injection conditions, as expected. It is commonly found in Cu(In, Ga)Se<sub>2</sub> that metastable defects exist, which metastably change their charge state with excitation. They even convert from donors to acceptors upon the quasi-Fermi level or minority carriers (electrons) density.<sup>[66–69]</sup> One of the most well-known metastable defects is the  $V_{\text{Se}}-V_{\text{Cu}}$  double vacancy that can convert from a shallow donor to a shallow acceptor with illumination.<sup>[1]</sup> This metastable defect transition increases the net doping level and makes  $\frac{d \ln N_A}{d \ln G} > 0$  in Equation (7), thus leading to the ODF larger than 1 in low injection conditions.<sup>[8]</sup> In the following, we are going to show the influences of doping density and back surface recombination on the ODF. Some studies have pointed out that surface recombination is injection level dependent,<sup>[70,71]</sup> which means the linear assumption,  $\Delta n \propto G$ , may not be proper for samples that have high surface recombination. In this case, the assumption of “ $d \ln n / d \ln G = 1$ ” is not valid since  $\tau_n^{\text{eff}}(G)$  is a function of generation rather than a constant. Therefore, Equation (5) rather than Equation (7) is proper to describe the ODF in low injection conditions.

### 2.2.2. Experiment and SCAPS Simulation Results

To study the influence of back surface recombination on the ODF, as shown in Figure 6a, the generation flux-dependent PL flux of the dielectric layer passivated samples and their reference are measured. The ODF is determined by using a single power law fitting, i.e., assuming a constant ODF, which is a good approximation since the measurements are carried out only over a bit more than 2 orders of magnitude of generation around one Sun. The unpassivated reference sample has the smallest ODF around 1.10. The ODF increases to 1.15 when introducing a TiO<sub>2</sub> passivation layer. And a larger value of around 1.27 is obtained with Al<sub>2</sub>O<sub>3</sub> or glass back contact. Therefore, it appears that back surface recombination tends to reduce the ODF. A small diode factor is desirable to gain a good fill factor, but back surface recombination increases non-radiative recombination that causes the loss in  $V_{\text{oc}}$  and thus the efficiency. SCAPS simulations are conducted to understand the experimental observations, and the results are shown in Figure 6b,c. Because the doping density has an influence on the ODF which will be discussed later, we fix the doping density at  $8.8 \times 10^{15} \text{ cm}^{-3}$  which is similar to the experimental results (see Table 1). More parameters used in the SCAPS simulations can be found in Tables S1 and S2 (Supporting Information). Figure 6c shows the local ODF changes with generation.



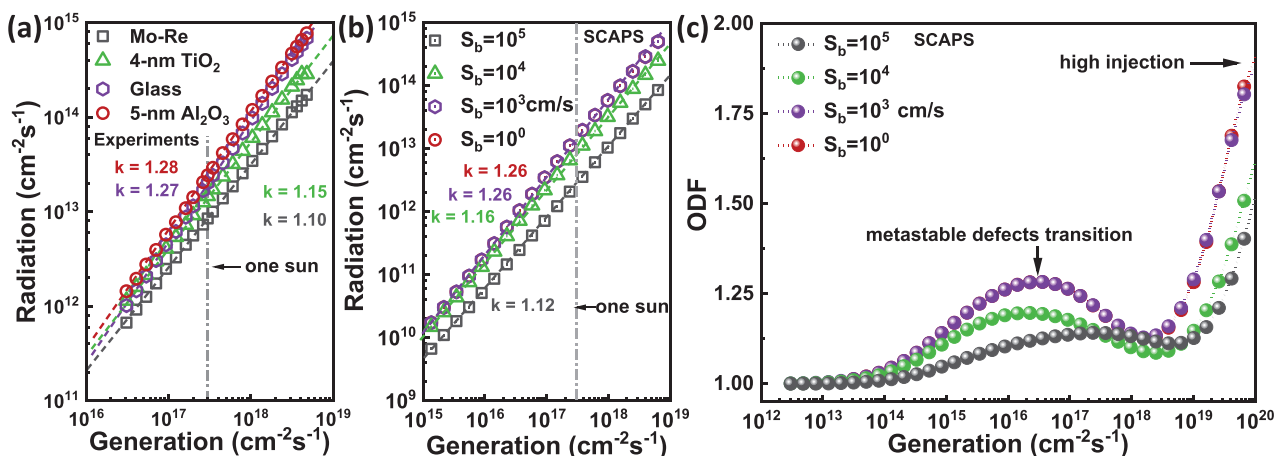


**Figure 6.** a) Generation flux-dependent radiation flux of the dielectric layer passivated series. b) The SCAPS simulated Radiation-Generation dependence. The curve with  $S_b = 10^0$  is not visible in (b) and (c) because it is almost the same as the curve with  $S_b = 10^3$   $\text{cm}^{-1}$ ; c) The SCAPS simulated local ODF over a wider range of generation fluxes: it changes with generation for different backside recombination velocities (doping density  $N_A = 8.8 \times 10^{15}$   $\text{cm}^{-3}$ , metastable defects density  $N_t = 8.0 \times 10^{15}$   $\text{cm}^{-3}$ ).

With a low generation flux below  $\approx 10^{16}$   $\text{cm}^{-2}$   $\text{s}^{-1}$ , the ODF increases with increasing generation flux because metastable donors convert increasingly to acceptors, thereby increasing the net doping. After the ODF reaches the maximum at around  $\approx 10^{16}$  to  $\approx 10^{17}$   $\text{cm}^{-2}$   $\text{s}^{-1}$ , it starts to reduce back towards 1 because the number of metastable donors, available for the transformation, decreases with the increasing generation flux. When generation flux is beyond  $\approx 10^{19}$   $\text{cm}^{-2}$   $\text{s}^{-1}$ , an increase in the ODF towards 2 indicates the beginning of high injection where the excited carriers are enough to shift both  $E_{\text{fm}}$  and  $E_{\text{fp}}$ . With the increase in back surface recombination velocity, the peak of the local ODF as a function of generation flux becomes lower and flatter, indicating that back surface recombination reduces the ODF. Because the local ODF peak in the one-Sun generation range is broad enough, the simulated Radiation-

Generation characteristic in Figure 6b can be fitted by a single power law approximation that agrees with our experimental results. The simulated ODFs shown in Figure 6b demonstrate that back surface recombination reduces the ODF from 1.26 to 1.12 when back surface recombination velocity increases from 1 to  $10^5$   $\text{cm}^{-1}$ . The simulated ODF with the  $S_b$  of 10 and  $10^2$   $\text{cm}^{-1}$  are not shown since they are almost the same as the situation with the  $S_b$  of  $10^3$   $\text{cm}^{-1}$ , i.e., a back surface recombination velocity of  $10^3$   $\text{cm}^{-1}$  or lower does not influence the ODF. The simulation indicates an ODF of 1.26 with a low  $S_b$  at the order of  $10^3$   $\text{cm}^{-1}$  or below. This is nearly the same as the experimentally determined ODF of  $\text{Al}_2\text{O}_3$  (1.27) and glass (1.28) samples that have the  $S_b$  in the same order ( $S_b[\text{Al}_2\text{O}_3] = 1.2 \times 10^3$   $\text{cm}^{-1}$ ,  $S_b[\text{Glass}] = 5.9 \times 10^3$   $\text{cm}^{-1}$  as summarized in Table 1). With a higher  $S_b$  of  $10^4$   $\text{cm}^{-1}$ , the simulated ODF reduces to 1.16

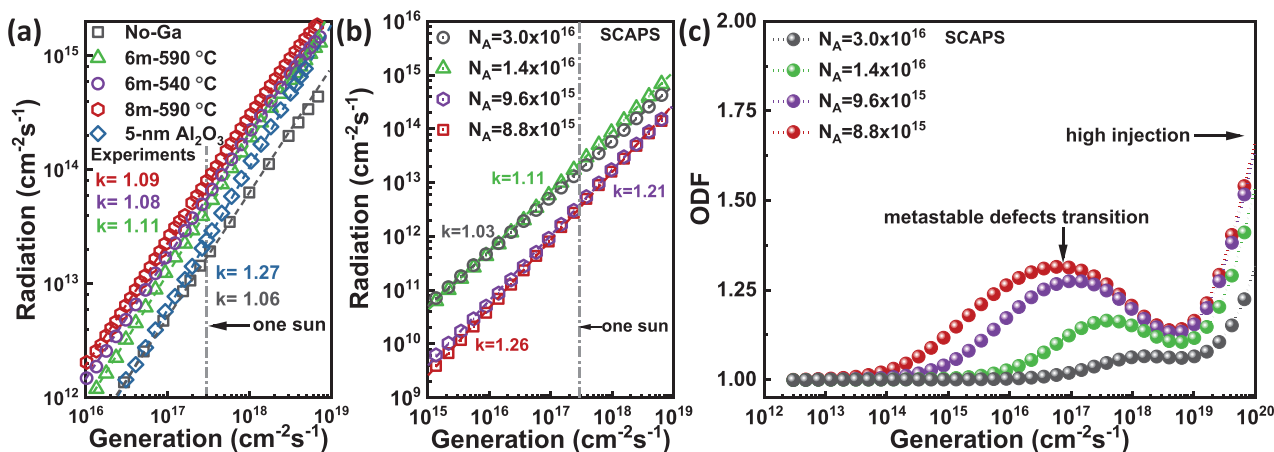


**Figure 7.** a) Generation-dependent radiation characteristics of no-Ga and GBG samples. The higher doping density of  $\approx 1.8 \times 10^{16}$   $\text{cm}^{-3}$  results in a small ODF close to 1.1. To show the influence of doping density on the ODF, a lower doped  $\text{Al}_2\text{O}_3$  passivated sample with the ODF of 1.27 is added; b) The SCAPS simulated Radiation-Generation characteristics are in good agreement with our experimental results; c) With fixed  $S_b = 10^2$   $\text{cm}^{-1}$ , the local ODF from SCAPS simulations becomes lower and shifts to high injection level with an increase in doping density.

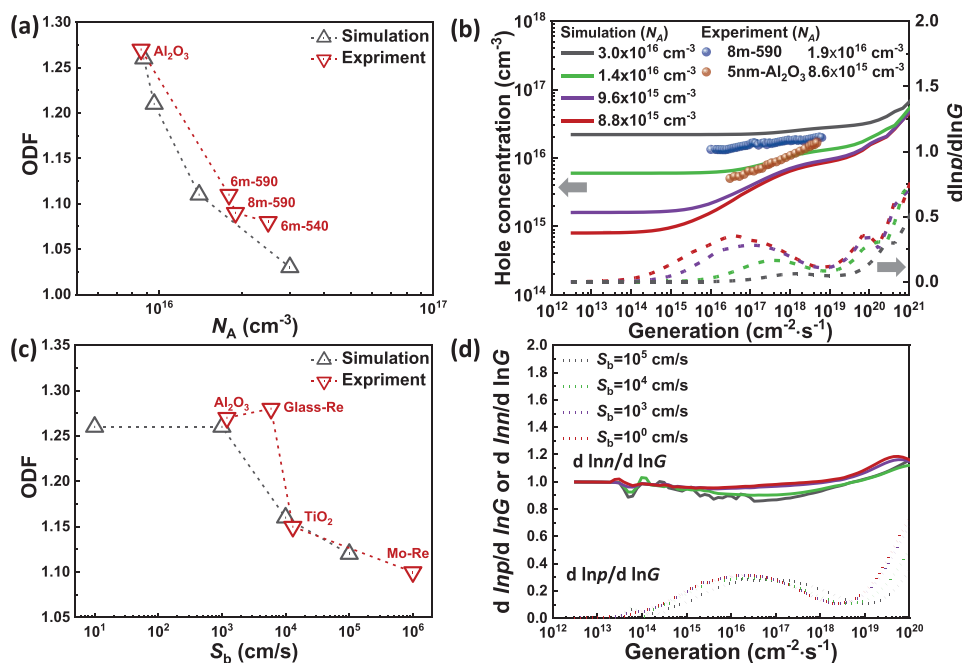


**Figure 8.** a,c) The ODF due to metastable defects is reduced by an increase in doping density or back surface recombination. b) The influence of doping density on the hole density with respect to generation flux in the presence of metastable defects. The solid lines are the hole densities from the simulations, spheres are experimentally determined values according to Equation (3). The dashed lines are the simulated “ $d \ln p / d \ln G$ ”, i.e., the ODF according to Equation (7); d) Simulation results of “ $d \ln n / d \ln G$ ” (solid lines) and “ $d \ln p / d \ln G$ ” (dashed lines) with different  $S_b$ . The back surface recombination increases with injection level, which decreases “ $d \ln n / d \ln G$ .” The simulated “ $d \ln n / d \ln G$ ” or “ $d \ln p / d \ln G$ ” is taken from the middle of the absorber.

which is similar to our experimental result of 1.15 for the  $\text{TiO}_2$  sample with the  $S_b$  around  $1.3 \times 10^4 \text{ cm s}^{-1}$ . And both experiment and simulation give us the smallest ODF around 1.11 when back surface recombination velocity reaches  $10^5 \text{ cm s}^{-1}$  or above. Therefore, a small ODF close to 1 could be a result of serious backside recombination that leads to higher  $\Delta E_F$  deficits, thus lower efficiency.

As discussed above, taking rather low  $S_b$  of GBG samples into account, their ODF could be expected to be almost the same as dielectric layer passivated samples. However, as shown in Figure 7a, the measured ODFs of the GBG samples are as small as 1.10. We believe this is because of the higher doping density of the GBG samples ( $1.8 \times 10^{16} \text{ cm}^{-3}$ ) compared to dielectric layer passivated samples ( $8.0 \times 10^{15} \text{ cm}^{-3}$ ). The samples with higher doping density have a higher hole density reservoir. Assuming the same amount of metastable donors that can transform into acceptors, their effect on a higher (dark) doping density is relatively smaller. It reduces the dynamic process (“ $d \ln p / d \ln G$ ”) and thus the ODF. This is also demonstrated by SCAPS simulations, shown in Figure 7c, where the local ODF peak becomes lower and shifts to a higher injection level with an increase in doping density. The simulated ODFs around one sun illumination, shown in Figure 7b, demonstrate that the ODF decreases from 1.26 to 1.03 when the doping density increases from  $8.8 \times 10^{15} \text{ cm}^{-3}$  to  $3.0 \times 10^{16} \text{ cm}^{-3}$ .

In conclusion, both experiment and simulation results demonstrate that serious back surface recombination and high doping density lead to a small ODF. Therefore, it is important to be aware that a small ODF can be realized by both back surface recombination and doping density. Serious back surface

recombination reduces the ODF by increasing non-radiative recombination which results in higher  $\Delta E_F$  deficits, thus lower  $V_{oc}$  and efficiency. On the contrary, the higher doping density reduces the ODF with increasing radiative recombination, which leads to a higher  $\Delta E_F$ , thus a higher  $V_{oc}$  and efficiency.

### 2.2.3. Discussion about the Influence of $S_b$ and $N_A$ on the ODF

As discussed above, both experiment and simulation results show that a higher doping density results in a smaller ODF, which is summarized in Figure 8a. The reason behind this is shown in Figure 8b. Generally, the net doping density (hole density) increases upon increasing generation due to metastable donors converting to acceptors, leading to “ $d \ln p / d \ln G > 0$ ” (or “ $d \ln N_A / d \ln G > 0$ ”) and thus the ODF  $> 1$  in low injection conditions. Figure 8b shows the simulated and hole density ( $p$ ) in the middle of the absorber. As shown in Figure S11 (Supporting Information), the ODFs obtained at different positions of the absorber are essentially the same, which means the ODF originating from metastable defects transition does not depend on the position within the absorber. With the same amount of extra holes gained from metastable defects transition, the relative increase in hole density for the higher doped samples is less than the lower doped samples as shown in Figure 8b by solid lines. Thus, “ $d \ln p / d \ln G$ ” becomes smaller in the highly doped samples as shown in Figure 8b by dashed lines, resulting in a smaller ODF. When generation fluxes are low, the net doping density is lower than  $N_A$  because of the ionized metastable donors.

With low back surface recombination, the minority carrier lifetime only weakly depends on generation flux. According to Equation (3), for the 8m-590 and  $\text{Al}_2\text{O}_3$  samples, the hole density as a function of generation flux is shown in Figure 8b by sphere symbols. The hole density in both samples increases considerably with generation flux, although it is well within the low excitation regime, which confirms the metastable donors converting to acceptors. The GBG sample (8m-590) has a higher doping density corresponding to a smaller " $d \ln p / d \ln G$ ," thus a smaller ODF. On the contrary, the lower doped  $\text{Al}_2\text{O}_3$  passivated sample has a lower hole reservoir but a larger " $d \ln p / d \ln G$ " which leads to a larger ODF. In low generation regions, only a small fraction of metastable donors transform into acceptors, meaning that net doping is still mostly determined by dark doping. It dominates the radiation flux that is proportional to net doping density. As a result, when the generation flux is very low, the higher doped samples have a higher radiation flux than the lower doped sample (Figure 7a). But with an increase in generation flux, the radiation fluxes are getting closer because the additional holes from metastable defect transitions minimize the difference in net doping density. This convergence behavior of the Radiation-Generation characteristics is observed for both experiments and simulations as shown in Figure 7a,b.

Besides the influence of doping density, serious back surface recombination reduces the ODF as summarized in Figure 8c. An obvious explanation would be based on the fact that the metastable defect transitions are dependent on the electron quasi-Fermi level, i.e., free electron density. Because the electrons are removed by back surface recombination, fewer free electrons can be captured by metastable donors to generate acceptors (see Figure S12, Supporting Information), which could be expected to reduce the ODF. Higher backside recombination means a high generation flux is needed to achieve the same electron occupation level, which shifts the " $d \ln p / d \ln G$ " dependence to higher generation fluxes as shown in Figure 8d with the dashed lines. But as long as there are enough free electrons, the electron occupation or " $d \ln p / d \ln G$ " can reach the same maximum independent of  $S_b$ . Thus the reduced availability of photoelectrons is unable to explain a lower ODF due to a higher  $S_b$ , as observed by experiments and simulations in Figure 6. Only a shift in the " $d \ln p / d \ln G$ " towards higher generation fluxes can be explained, not the smaller local ODF as shown in Figure 6c. However, as seen in Figure 8d (solid lines), besides the shift of " $d \ln p / d \ln G$ ," a high  $S_b$  also reduces " $d \ln n / d \ln G$ ," which explains the smaller ODF according to Equation (5). It means a sublinear increase in minority carrier concentration upon generation, which indicates generation-dependent backside recombination. This dependence can be explained by changes in the transport of minority carriers towards the back contact which becomes generation dependent because it depends on a band bending towards the back contact that is related to the metastable defects transitions. A detailed discussion is given in Section S14 (Supporting Information). The sublinear increase of minority carriers with generation flux is only observed in the case where metastable defects are present. Thus both the fact that  $\text{ODF} > 1$  and its decrease with increasing backside recombination are due to the presence of metastable defects.

When the injection level is very low, the recombination is dominated by SRH recombination in the bulk with less impact of backside recombination due to the low free electron density. As a result, all samples with the same bulk but different back side recombination have more or less the same radiation flux as shown in Figure 6a,b. With the increase of generation flux, the backside recombination becomes more effective, more so for samples with high backside recombination velocity, which results in a larger difference in radiation flux, thus diverging Radiation-Generation characteristics. Thus samples that differ mostly by surface recombination will demonstrate diverging Radiation-Generation characteristics, whereas samples that differ mostly in doping level will exhibit converging Radiation-Generation characteristics. These observations may help to distinguish the dominating recombination channels in solar cells because it suggests that not only the value of ODF, but the behavior of Radiation-Generation characteristics can help us distinguish whether the smaller ODF originates from a higher doping density that is beneficial to efficiency or from (back) surface recombination that is detrimental.

### 3. Conclusion

In this work, using  $\text{Cu(In, Ga)Se}_2$  solar cells as an example, photoluminescence is used to quantify doping density and back surface recombination velocity. The PL is a nondestructive optical method that allows us to study the performance of solar cells without finishing the whole device, which is flexible and reliable. First, we quantified the influence of backside recombination on  $\Delta E_F$ . Both Ga back grading and a dielectric layer ( $\text{Al}_2\text{O}_3$  as the best) increase  $\Delta E_F$  by around 40 meV compared to their reference samples without passivation, indicating that the passivation effect of a Ga gradient is as efficient as that of dielectric layers. The passivation effects are also confirmed by longer  $\tau_n^{\text{eff}}$  of both types of passivated samples. The sample series with dielectric layers show longer  $\tau_n^{\text{eff}}$ , yet lower  $\Delta E_F$  compared to the GBG sample series because of the lower (dark) doping density. Based on experimental results of  $\Delta E_F$ ,  $\tau_n^{\text{eff}}$ , and doping density, both simulation and analytical analysis are utilized to quantify surface recombination velocity, which makes it possible to directly compare the passivation effects of different strategies through recombination velocity. We believe it is a general approach that can be extended to any solar cell materials to quantify surface recombination velocity, which gives a deeper understanding of the influence of surface recombination on devices' performance. In particular, we show that both, dielectric layers and a suitable Ga gradient reduce back surface recombination by three orders of magnitude. The further reduction would only be effective for absorbers with a longer bulk lifetime.

Having quantified doping density and surface recombination velocity, their relationship with the diode factor is studied. On the one hand, both experiment and simulation results show that increased surface recombination leads to a smaller ODF but by effects that are undesirable and detrimental to the performance of solar cells. On the other hand, a smaller ODF due to the higher doping density is beneficial to improving  $\Delta E_F$  and hence performance of solar cells. Therefore both increase in radiative and non-radiative recombination can result in a

smaller ODF. Combining  $\Delta E_F$  and the behavior of Radiation-Generation characteristics with the ODF can help us distinguish dominated recombination channels underlying. For samples with lower  $\Delta E_F$  and diverging Radiation-Generation characteristics, i.e., increasing  $\Delta E_F$  deficits upon generation, back surface recombination is likely the crucial factor for high  $\Delta E_F$  deficits. The converging Radiation-Generation characteristics suggest that low doping density may dominate the high  $\Delta E_F$  deficits. Besides these concrete consequences for the development of solar cell absorbers, the dependence of the ODF on the doping density gives further support to the model that explains ODF >1 is caused by metastable defect transitions.

## 4. Experimental Section

**Sample Preparing:** Except for the sample directly grown on clean soda lime glass, preparation of other samples begins with sputtered molybdenum (Mo) coated soda lime glass, the thickness of the Mo layer is around 500 nm. For the dielectric metal oxides layer passivated sample, a  $\text{TiO}_2$  or  $\text{Al}_2\text{O}_3$  was deposited on the Mo layer using atomic layer deposition (ALD) processes. The  $\text{Al}_2\text{O}_3$  layers were deposited by plasma-assisted ALD at 200 °C substrate temperature using trimethyl aluminum (TMA) as an aluminum precursor and an inductively coupled remote oxygen plasma for oxidation. The growth rate of the applied plasma-assisted ALD process is 1.2 Å per cycle. With 42 cycles, it corresponds to  $\text{Al}_2\text{O}_3$  layer thicknesses of 5 nm. The  $\text{TiO}_x$  layers were deposited using thermal ALD (FlexAl reactor, Oxford Instruments), again at the substrate temperature of 200 °C. Tetrakis (dimethylamino) titanium (TDMAT),  $\text{H}_2\text{O}$  and  $\text{N}_2$  are used as the titanium precursor, oxidant and purge gases, respectively. The layer thicknesses as determined from the growth rate of 0.43 Å per cycle and 100 cycles amount to 4 nm.

**Dielectric Metal Oxide Layer Sample Series:** Polycrystalline  $\text{CuInSe}_2$  thin films with a thickness of  $\approx 2.0 \mu\text{m}$  were grown by a molecular beam epitaxy (MBE) system by a one-stage process which means Cu, In and Se molecular fluxes were supplied at the same time. The substrate setting temperature is 550 °C for the first 15 min, then increases to 590 °C for the rest of the process (see also Figure S14a, Supporting Information). The sample was directly grown on glass and Mo experienced the same deposition process as the dielectric layer passivated samples. The Cu/In ratio determined by energy dispersive X-ray spectroscopy (EDX) is around 0.87.

**GBG Sample Series:** Polycrystalline  $\text{Cu(In, Ga)Se}_2$  thin films were prepared with a one-stage process. 6 or 8 min of  $\text{CuGaSe}_2$  was deposited before  $\text{CuInSe}_2$  deposition (see Figure S15b, Supporting Information). Three different samples were prepared: 6m-590/8m-590/6m-540 sample means 6/8/6 min predeposition of  $\text{CuGaSe}_2$  with substrate setting temperatures of 550/550/500 °C. Then followed by 15 min of  $\text{CuInSe}_2$  deposition at the same temperature and 55 min of  $\text{CuInSe}_2$  deposition at a higher substrate temperature of 590/590/540 °C. Regarding the reference sample, it experienced the same deposition process as high substrate temperature prepared samples (550/590 °C) but without pre-deposition of  $\text{CuGaSe}_2$ . These samples have a thickness between 1.2  $\mu\text{m}$  to 1.5  $\mu\text{m}$  and an EDX-determined Cu/(In+Ga) ratio of 0.96. Changing Ga supply duration and substrate temperature leads to different profiles.

Before the chemical bath deposited (CBD) CdS buffer was applied to cover the absorber surface, all samples were chemically etched with 5% aqueous KCN solution for 30 s to remove potential residual oxides.<sup>[72]</sup> The standard CBD recipe is 6–7 min deposition at 67 °C with  $2 \times 10^{-3}$  M  $\text{CdSO}_4$ ,  $50 \times 10^{-3}$  M thiourea, and 1.5 M  $\text{NH}_4\text{OH}$ . The estimated thickness is 40–50 nm according to typical growth rates. The CdS is necessary to passivate the front surface and prevent surface degradation during the PL characterization.<sup>[38,43,44]</sup> Additionally, placing the CdS covered samples on the 200 °C hot plate for 2 min in the air was performed to further improve the  $\Delta E_F$ .

**Devices:** Because the dielectric layers block the transport of carriers which results in a rather low short-circuit current density ( $J_{sc}$ ),<sup>[62,63]</sup> devices were only made for GBG samples. To complete the devices, a sputtered double layer of i-ZnO/AZO and e-beam evaporated Ni/Al electrodes were deposited in sequence.

**Characterization: Absolute PL:** The PL system is a home-built setup. All samples were excited by a 660 nm diode laser with a spot diameter of  $\approx 2.6$  mm in the air at room temperature. The emitted photoluminescence was collected by two parabolic mirrors and then redirected to a monochromator before transmitting to an InGaAs detector with a 550  $\mu\text{m}$  optical fiber. The PL spectra used for the  $\Delta E_F$  and ODF determination were corrected by a calibrated halogen lamp. Quantification of both excitation and radiation flux was done by a power meter, which allows us to calculate  $\Delta E_F$  with specific illumination intensities from 0.01 sun, even lower, to dozens of sun equivalents, depending on the quality and  $E_g$  of absorbers. One sun means the photon flux equals to AM1.5 spectrum depending on the  $E_g$  of the absorber. According to Planck's generalized law with the Boltzmann approximation,<sup>[48]</sup> the  $\Delta E_F$  can be calculated by fitting the high energy wing of the PL spectra where the absorbance is assumed equal to 1 ( $a(E) = 1$ ) with the temperature fixed to the measured temperature of 296 K. More details about calculation can be found in other works.<sup>[44,73–75]</sup>

**Time-Resolved PL (TRPL):** This technology is based on time-correlated single photon counting (TCSPC) which is used to measure luminescence decays in the time domain. Measurements were taken with a 640 nm pulsed diode laser. Because some of the samples do not follow the 1-exponential decay, the weighted effective lifetime is adopted, which is calculated via:

$$\tau_e = \frac{A_1\tau_1 + A_2\tau_2}{A_1 + A_2} \quad (8)$$

where  $A_1$  and  $A_2$  are the prefactor for the  $\tau_1$  and the  $\tau_2$ , respectively. Where possible, lifetimes with a 1-exponential decay function are also fitted and the results are also summarized in Table S3 (Supporting Information). Because the difference between the 1-exponential estimated lifetime compared to the weighted effective lifetime is negligible, the weighted effective lifetime is used for the discussions.

**Illumination and Dark J–V:** Measurements were carried out at 25 °C in a 4-probe configuration with a class AAA solar simulator that supplies a simulated AM1.5G spectrum calibrated by a Si reference cell. The forward scanning voltage is applied from -0.3 V to 0.6 V with a step of 0.01 V.

**Secondary Ion Mass Spectrometry (SIMS) Depth Profiles:** Measurements were performed with a CAMECA SC-ultra instrument (Ametek). 1 keV focused  $\text{Cs}^+$  ion beam (5 nA) was applied to sputter over a surface of the sample with an area of 250  $\mu\text{m} \times 250 \mu\text{m}$ . Only ions from the center with an area of 60  $\mu\text{m}$  in diameter were detected as  $\text{MCs}^+$  or  $\text{MCs}_2^+$  where M stands for interested ions such as Cu, In, Ga, Se, and Mo.

**Energy Dispersive X-ray Spectroscopy (EDX):** EDX was introduced to determine the overall composition of the  $\text{Cl(G)Se}_2$  with an electron acceleration voltage of 20 kV. To obtain quantified results, the spectrum of each element was calibrated by their standard spectrum measured with the same electron acceleration voltage.

**SCAPS Simulation Setups:** SCAPS<sup>[34]</sup> is mainly used for device simulations, but it is still possible to study  $\Delta E_F$  and ODF of a single semiconductor layer. The  $\Delta E_F$  can be extracted by considering the difference between electron and hole quasi-Fermi level ( $\Delta E_F = E_F^n - E_F^p$ ). The ODF simulations are conducted by changing the neutral density (ND) setting which can give illumination or generation flux from  $1 \times 10^{12}$  to  $1 \times 10^{21} \text{ cm}^{-2} \text{ s}^{-1}$ .

SCAPS does not directly give us radiation flux. But if the number of photons is equalled emitted via radiation to the number of electrons that recombine radiatively, the radiation flux can be calculated by the radiative

recombination current density,  $R_r = \frac{J_r}{q}$ , where  $R_r$  is the radiation flux,  $J_r$  is

the radiation recombination current density and  $q$  is the elementary charge. All parameters used in these simulations are state-of-art values that can be found in other works<sup>[8]</sup> and summarized (Tables S1 and S2, Supporting Information). And it is worth mentioning several specific settings:



1. The sample structure is: front contact/1 nm defect-free CuInSe<sub>2</sub>/1 or 3 μm CuInSe<sub>2</sub>/1 nm defect-free CuInSe<sub>2</sub>/back contact. The thin defects-free layers at both sides are introduced to get rid of band bending due to charged defects. This band bending results in artificial results of the ODF in the simulation setups. Standard is 3 μm thick CuInSe<sub>2</sub>. The 1 μm CuInSe<sub>2</sub> is only used to simulate the influence of back surface recombination on the ODF because the thinner CuInSe<sub>2</sub> shows a more obvious effect.
2. The effective radiative recombination coefficient in this work is found by adjusting the radiative recombination flux equal to the generation flux under the one sun where the radiative recombination is kept as the only recombination channel (i.e., all surface recombination velocities = 0 and no defects) and make  $\Delta E_F$  equals to  $\Delta E_F^{SQ}$ .<sup>[21]</sup>

$$R_r = \frac{J_r}{q} = G = d \cdot B n_i^2 \exp\left(\frac{\Delta E_F^{SQ}}{k_B T}\right) \quad (9)$$

where  $G$  is the generation flux,  $d$  is the thickness of the absorber,  $B$  is the effective radiative recombination coefficient and  $n_i$  is the intrinsic charge carrier density. As a result, the SCAPS simulator gives us a thickness-dependent effective radiative recombination coefficient, as shown in Table S1 (Supporting Information), that is nearly 3 orders of magnitude smaller than the actual radiative recombination coefficient.<sup>[76]</sup> One reason for this is that the model used here does not completely satisfy the assumption of the SQ model: a step function of absorptivity, infinite carrier mobility or zero absorber thickness. Another important reason is that the radiation flux given by SCAPS is an internal radiation flux without considering the effects of light outcoupling and photon recycling. The photon recycling occurs because the interface only allows photons within the escape cone to be emitted, the rest of them are reflected back into the absorber and absorbed again. With this effect, the internal radiation flux gained from SCAPS simulator is a factor of  $4n^2$  larger than the external radiation flux, where  $n$  is the refractive index.<sup>[22]</sup> To take both effects of the deviation from the SQ model and the difference between internal and external photon flux into account, this smaller effective  $B$  is used in all simulations.

3. Metastable defects are included with a density of  $8 \times 10^{15} \text{ cm}^{-3}$  that is comparable to the net doping density which changes from  $8.8 \times 10^{15} \text{ cm}^{-3}$  to  $3 \times 10^{16} \text{ cm}^{-3}$ . This is especially important for the metastable transition theory discussed in Section 2.2 because only when the amount of holes gained from metastable defects converting is comparable to the net doping density, it is possible to observe the ODF larger than 1 in the low injection regions. For metastable defects setting, the energetic position of the donor state is at the middle of the bandgap, and the acceptor state is located at 0.2 eV above the valence band edge. Setting both of them as shallow defects always results in problems of convergence in the simulations. It is also very important to know that these metastable configurations only work when considering the equilibrium of the absorber for each illumination intensity. It means in the “batch” setup of SCAPS, the measurement working point and initial working point of different illumination intensities should be selected and simulated at the same time.
4. There are no interface defects set between defect-free CuInSe<sub>2</sub> and CuInSe<sub>2</sub>, the surface recombination velocity is modified by directly changing the surface recombination velocity in the contacts setting.

## Supporting Information

Supporting Information is available from the Wiley Online Library or from the author.

## Acknowledgements

This work was supported by the Luxembourg National Research Fund (FNR) through the PACE project under the grant number PRIDE17/12246511/PACE and through the SeVac project

(C17/MS/11655733/SeVac) and the GRISC project (C17/MS/11696002 GRISC). The authors thank all developers of SCAPS at the department of Electronics and Information Systems (ELIS) of the University of Gent. Brahime El Adib is thanked for his technical assistance for SIMS measurements performed within the Advanced Characterization Platform (LIST). For the purpose of open access, the author has applied a Creative Commons Attribution 4.0 International (CC BY 4.0) license to any Author Accepted Manuscript version arising from this submission.

## Conflict of Interest

The authors declare no conflict of interest.

## Data Availability Statement

The data that support the findings of this study are openly available in Zenodo at <https://doi.org/10.5281/zenodo.5813052>, reference number 5813052.

## Keywords

back contacts, CIGSe, optical diode factor, photoluminescence

Received: June 20, 2022  
Revised: September 4, 2022  
Published online:

- [1] S. Lany, A. Zunger, *J. Appl. Phys.* **2006**, *100*, 113725.
- [2] A. Nagaoka, D. Kuciauskas, M. A. Scarpulla, *Appl. Phys. Lett.* **2017**, *111*, 232103.
- [3] K. Bothe, R. Hezel, J. Schmidt, *Appl. Phys. Lett.* **2003**, *83*, 1125.
- [4] K. Macielak, M. Maciaszek, M. Igalson, P. Zabierowski, N. Barreau, *IEEE J. Photovoltaics* **2015**, *5*, 1206.
- [5] V. P. Markevich, M. Vaqueiro-Contreras, J. T. De Guzman, J. Coutinho, P. Santos, I. F. Crowe, M. P. Halsall, I. Hawkins, S. B. Lastovskii, L. I. Murin, A. R. Peaker, *Phys. Status Solidi A* **2019**, *216*, 1900315.
- [6] G. Baraff, M. Schluter, *Phys. Rev. Lett.* **1985**, *55*, 2340.
- [7] T. Theis, P. Mooney, S. Wright, *Phys. Rev. Lett.* **1988**, *60*, 361.
- [8] T. P. Weiss, F. Ehre, V. Serrano-Escalante, T. Wang, S. Siebentritt, *Sol. RRL* **2021**, *5*, 2100063.
- [9] R. Scheer, H.-W. Schock, *Chalcogenide Photovoltaics: Physics, Technologies, and Thin Film Devices*, John Wiley & Sons, New York **2011**.
- [10] T. Kirchartz, J. A. Márquez, M. Stollerfoht, T. Unold, *Adv. Energy Mater.* **2020**, *10*, 1904134.
- [11] S. Siebentritt, T. P. Weiss, M. Sood, M. H. Wolter, A. Lomuscio, O. Ramirez, *J. Phys. Mater.* **2021**, *4*, 042010.
- [12] Z. Hameiri, P. Chaturvedi, K. R. McIntosh, *Appl. Phys. Lett.* **2013**, *103*, 023501.
- [13] T. Kirchartz, U. Rau, *Adv. Energy Mater.* **2018**, *8*, 1703385.
- [14] T. Kirchartz, F. Deledalle, P. S. Tuladhar, J. R. Durrant, J. Nelson, *J. Phys. Chem. Lett.* **2013**, *4*, 2371.
- [15] J. Malmström, J. Wennerberg, L. Stolt, *Thin Solid Films* **2003**, *431*, 436.
- [16] W. Tress, M. Yavari, K. Domanski, P. Yadav, B. Niesen, J. P. C. Baena, A. Hagfeldt, M. Graetzel, *Energy Environ. Sci.* **2018**, *11*, 151.
- [17] P. Calado, D. Burkitt, J. Yao, J. Troughton, T. M. Watson, M. J. Carnie, A. M. Telford, B. C. O'Regan, J. Nelson, P. R. Barnes, *Phys. Rev. Appl.* **2019**, *11*, 044005.

- [18] T. Trupke, R. Bardos, M. Abbott, J. Cotter, *Appl. Phys. Lett.* **2005**, *87*, 093503.
- [19] F. Babbe, L. Choubrac, S. Siebentritt, *Sol. RRL* **2018**, *2*, 1800248.
- [20] V. Sarritzu, N. Sestu, D. Marongiu, X. Chang, S. Masi, A. Rizzo, S. Colella, F. Quochi, M. Saba, A. Mura, *Sci. Rep.* **2017**, *7*, 44629.
- [21] W. Shockley, H. J. Queisser, *J. Appl. Phys.* **1961**, *32*, 510.
- [22] P. Würfel, *J. Phys. C: Solid State Phys.* **1982**, *15*, 3967.
- [23] T. P. Weiss, B. Bissig, T. Feurer, R. Carron, S. Buecheler, A. N. Tiwari, *Sci. Rep.* **2019**, *9*, 5385.
- [24] M. Nichterwitz, T. Unold, *J. Appl. Phys.* **2013**, *114*, 134504.
- [25] E. Jarzembowski, F. Syrowatka, K. Kaufmann, W. Fränzel, T. Hölscher, R. Scheer, *Appl. Phys. Lett.* **2015**, *107*, 051601.
- [26] T. Feurer, B. Bissig, T. P. Weiss, R. Carron, E. Avancini, J. Löckinger, S. Buecheler, A. N. Tiwari, *Sci Technol Adv Mater* **2018**, *19*, 263.
- [27] S. C. Yang, M. Ochoa, R. Hertwig, A. Aribia, A. N. Tiwari, R. Carron, *Prog. Photovoltaics: Res. Appl.* **2021**, *29*, 630.
- [28] T. Feurer, R. Carron, G. T. Sevilla, F. Fu, S. Pisoni, Y. E. Romanyuk, S. Buecheler, A. N. Tiwari, *Adv. Energy Mater.* **2019**, *9*, 1901428.
- [29] M. Nakamura, K. Yamaguchi, Y. Kimoto, Y. Yasaki, T. Kato, H. Sugimoto, *IEEE J. Photovoltaics* **2019**, *9*, 1863.
- [30] R. Kotipalli, B. Vermang, J. Joel, R. Rajkumar, M. Edoff, D. Flandre, *AIP Adv.* **2015**, *5*, 107101.
- [31] P. M. Salome, B. Vermang, R. Ribeiro-Andrade, J. P. Teixeira, J. M. Cunha, M. J. Mendes, S. Haque, J. Borme, H. Águas, E. Fortunato, *Adv. Mater. Interfaces* **2018**, *5*, 1701101.
- [32] G. Birant, J. de Wild, M. Meuris, J. Poortmans, B. Vermang, *Appl. Sci.* **2019**, *9*, 677.
- [33] F. Werner, B. Veith-Wolf, C. Spindler, M. R. Barget, F. Babbe, J. Guillot, J. Schmidt, S. Siebentritt, *Phys. Rev. Appl.* **2020**, *13*, 054004.
- [34] M. Burgelman, P. Nollet, S. Degraeve, *Thin Solid Films* **2000**, *361*, 527.
- [35] S. Shirakata, T. Nakada, *Thin Solid Films* **2007**, *515*, 6151.
- [36] I. Khatri, H. Fukai, H. Yamaguchi, M. Sugiyama, T. Nakada, *Sol. Energy Mater. Sol. Cells* **2016**, *155*, 280.
- [37] W. K. Metzger, I. L. Repins, M. A. Contreras, *Appl. Phys. Lett.* **2008**, *93*, 022110.
- [38] W. Metzger, I. Repins, M. Romero, P. Dippo, M. Contreras, R. Noufi, D. Levi, *Thin Solid Films* **2009**, *517*, 2360.
- [39] Y. Kamikawa, J. Nishinaga, H. Shibata, S. Ishizuka, *ACS Appl. Mater. Interfaces* **2020**, *12*, 45485.
- [40] T. P. Weiss, R. Carron, M. H. Wolter, J. Löckinger, E. Avancini, S. Siebentritt, S. Buecheler, A. N. Tiwari, *Sci. Technol. Adv. Mater.* **2019**, *20*, 313.
- [41] T. Feurer, F. Fu, T. P. Weiss, E. Avancini, J. Löckinger, S. Buecheler, A. N. Tiwari, *Thin Solid Films* **2019**, *670*, 34.
- [42] M. Gloeckler, A. Fahrenbruch, J. Sites, in *Proc. of 3rd World Conf. on Photovoltaic Energy Conversion*, (Ed.: K. Kurokawa), IEEE, Piscataway, NJ **2003**, p. 491.
- [43] D. Regesch, L. Gütay, J. K. Larsen, V. Deprédurand, D. Tanaka, Y. Aida, S. Siebentritt, *Appl. Phys. Lett.* **2012**, *101*, 112108.
- [44] F. Babbe, L. Choubrac, S. Siebentritt, *Appl. Phys. Lett.* **2016**, *109*, 082105.
- [45] A. Mudryi, V. Gremenok, A. Karotki, V. Zalesski, M. Yakushev, F. Luckert, R. Martin, *J. Appl. Spectrosc.* **2010**, *77*, 371.
- [46] S. Karthikeyan, S. Hwang, M. Sibakoti, T. Bontrager, R. W. Liptak, S. A. Campbell, *Appl. Surf. Sci.* **2019**, *493*, 105.
- [47] X. Wang, S. S. Li, W. Kim, S. Yoon, V. Craciun, J. Howard, S. Easwaran, O. Manasreh, O. Crisalle, T. Anderson, *Sol. Energy Mater. Sol. Cells* **2006**, *90*, 2855.
- [48] P. Würfel, *Physics of Solar Cells*, Wiley-VCH, Weinheim **2005**.
- [49] F. Mollica, J. Goffard, M. Jubault, F. Donsanti, S. Collin, A. Cattoni, L. Lombez, N. Naghavi, in *2016 IEEE 43rd Photovoltaic Specialists Conf. (PVSC)*, (Ed.: T. Anderson), IEEE, Piscataway, NJ **2016**, p. 2213.
- [50] J. Van Delft, D. Garcia-Alonso, W. Kessels, *Semicond. Sci. Technol.* **2012**, *27*, 074002.
- [51] C. L. Perkins, T. Ablekim, T. M. Barnes, D. Kuciauskas, K. G. Lynn, W. Nemeth, M. O. Reese, S. K. Swain, W. K. Metzger, *IEEE J. Photovoltaics* **2018**, *8*, 1858.
- [52] A. Ghods, V. G. Saravade, C. Zhou, I. T. Ferguson, *J. Vac. Sci. Technol., A* **2020**, *38*, 012406.
- [53] L. Zhang, Q. He, W.-L. Jiang, F.-F. Liu, C.-J. Li, Y. Sun, *Sol. Energy Mater. Sol. Cells* **2009**, *93*, 114.
- [54] A. Sproul, *J. Appl. Phys.* **1994**, *76*, 2851.
- [55] F. Werner, D. Colombara, M. Melchiorre, N. Valle, B. El Adib, C. Spindler, S. Siebentritt, *J. Appl. Phys.* **2016**, *119*, 173103.
- [56] A. Gerhard, W. Harneit, S. Brehme, A. Bauknecht, U. Fiedeler, M. C. Lux-Steiner, S. Siebentritt, *Thin Solid Films* **2001**, *387*, 67.
- [57] S. Siebentritt, L. Gütay, D. Regesch, Y. Aida, V. Deprédurand, *Sol. Energy Mater. Sol. Cells* **2013**, *119*, 18.
- [58] C. Stephan, S. Schorr, M. Tovar, H.-W. Schock, *Appl. Phys. Lett.* **2011**, *98*, 091906.
- [59] C. Spindler, F. Babbe, M. H. Wolter, F. Ehré, K. Santhosh, P. Hilgert, F. Werner, S. Siebentritt, *Phys. Rev. Mater.* **2019**, *3*, 090302.
- [60] D. G. Buldu, J. de Wild, T. Kohl, G. Brammertz, G. Birant, M. Meuris, J. Poortmans, B. Vermang, *Phys. Status Solidi* **2020**, *217*, 2000307.
- [61] B. Vermang, V. Fjällström, X. Gao, M. Edoff, *IEEE J. Photovoltaics* **2013**, *4*, 486.
- [62] B. Vermang, V. Fjallstrom, X. Gao, M. Edoff, *IEEE J. Photovoltaics* **2014**, *4*, 486.
- [63] D. Ledinek, O. Donzel-Gargand, M. Sköld, J. Keller, M. Edoff, *Sol. Energy Mater. Sol. Cells* **2018**, *187*, 160.
- [64] P. Caprioglio, C. M. Wolff, O. J. Sandberg, A. Armin, B. Rech, S. Albrecht, D. Neher, M. Stollerfoht, *Adv. Energy Mater.* **2020**, *10*, 2000502.
- [65] Y. Sun, S. Lin, W. Li, S. Cheng, Y. Zhang, Y. Liu, W. Liu, *Engineering* **2017**, *3*, 452.
- [66] P. T. Erslev, J. W. Lee, W. N. Shafarman, J. D. Cohen, *Thin Solid Films* **2009**, *517*, 2277.
- [67] J. Bailey, G. Zapalac, D. Poplavsky, in *2016 IEEE 43rd Photovoltaic Specialists Conf. (PVSC)*, (Ed.: T. Anderson), IEEE, Piscataway, NJ **2016**, p. 2135.
- [68] J. Heath, J. Cohen, W. Shafarman, *Thin Solid Films* **2003**, *431*, 426.
- [69] M. Igalsen, M. Cwil, M. Edoff, *Thin Solid Films* **2007**, *515*, 6142.
- [70] A. Stephens, A. Aberle, M. Green, *J. Appl. Phys.* **1994**, *76*, 363.
- [71] A. G. Aberle, T. Lauinger, J. Schmidt, R. Hezel, *Appl. Phys. Lett.* **1995**, *66*, 2828.
- [72] Y. Hashimoto, N. Kohara, T. Negami, M. Nishitani, T. Wada, *Jpn. J. Appl. Phys.* **1996**, *35*, 4760.
- [73] M. H. Wolter, *Doctor thesis*, University of Luxembourg, **2019**.
- [74] L. Gütay, G. Bauer, *Thin Solid Films* **2009**, *517*, 2222.
- [75] T. Unold, L. Gütay, in *Advanced Characterization Techniques for Thin Film Solar Cells* (Eds: D. Abou-Ras, T. Kirchartz, U. Rau), John Wiley & Sons, New York **2011**, Ch. 7.
- [76] J. H. Werner, J. Mattheis, U. Rau, *Thin Solid Films* **2005**, *480*, 399.